ACS Chemical Neuroscience

pubs.acs.org/chemneuro

Research Article

Single-Particle Resolution of Copper-Associated Annular α-Synuclein Oligomers Reveals Potential Therapeutic Targets of Neurodegeneration

Olena Synhaivska, Shayon Bhattacharya, Silvia Campioni, Damien Thompson,* and Peter Niraj Nirmalraj*

Cite This: *ACS Chem. Neurosci.* 2022, 13, 1410−1421

Read Online

ACCESS | Metrics & More | Article Recommendations | Supporting Information

ABSTRACT: Metal ions stabilize protein−protein interactions and can modulate protein aggregation. Here, using liquid-based atomic force microscopy and molecular dynamics simulations, we study the concentration-dependent effect of Cu^{2+} ions on the aggregation pathway of α-synuclein (α-Syn) proteins, which play a key role in the pathology of Parkinson's disease. The full spectrum of α-Syn aggregates in the presence and absence of Cu^{2+} ions from monomers to mature fibrils was resolved and quantified at the gold−water interface. Raman spectroscopy confirmed the atomic force microscopy (AFM) findings on the heterogeneity in aggregated states of α-Syn. The formation of annular oligomers was exclusively detected upon incubating α-Syn with Cu^{2+} ions. Our findings emphasize the importance of targeting annular α-Syn protein oligomers for therapeutic intervention and their potential role as biomarkers for early detection and monitoring progression of neurodegeneration.

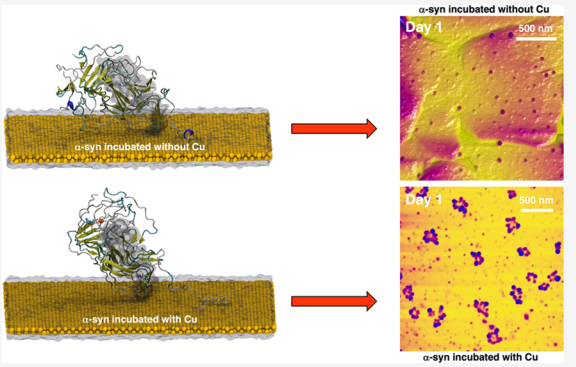

KEYWORDS: *neurodegeneration, peptide self-assembly, metal−protein interactions, atomic force microscopy, Raman spectroscopy, molecular dynamics simulations*

INTRODUCTION

The onset of Parkinson's disease (PD) occurs several years before the early symptoms of neurodegeneration become visible,[1] and it is estimated that at least 10 million people worldwide currently live with PD.[2] Genetic and environmental factors are majorly responsible for familial (inherited) and sporadic (caused by random gene−environment interactions) forms of PDs,[3] respectively. Excessive exposure to biometals such as iron, copper, and manganese may trigger or hasten PD.[4] Abnormal aggregation of the intrinsically disordered protein (IDP) α-synuclein (α-Syn, a 140-residue long neuronal protein) into amyloid fibrils precipitates the formation of intracellular inclusions termed Lewy bodies and Lewy neurites, which are the histopathological hallmarks of PD.[5] Misfolded and aggregated α-Syn has also been implicated in other neurodegenerative disorders[6] including Alzheimer's disease (AD),[7] with sensitive Luminex assays showing that α-Syn levels in cerebrospinal fluid (CSF) can be used as a diagnostic marker to distinguish between PD and AD patients.[7,8]

Elevated levels of metal ions present in α-Syn aggregates of patients suffering from PD suggest that metal homeostasis may play a significant role in the onset and progression of PD.[9] Especially, the postmortem brains of PD patients show raised levels of Cu(II) concentrations in CSF.[10] While α-Syn oligomers[11,12] are the known neurotoxic species in PD,[13] the development of effective anti-PD drugs requires targeting of specific structures arising in the early stages of α-Syn phase transitions[14] or the nucleation-dependent elongation[15] of oligomers into protofibrils. In parallel, advanced methods are required to routinely characterize the size and morphology of intermediary nano and microstructures formed during self-assembly and aggregation in the presence of aqueous metal ions to track disease progression in, *e.g.*, a blood test,[16] to provide effective personalized patient care.

Here, we visualize and quantify α-Syn aggregates on Au(111) prepared in buffer salt solution (phosphate buffer solution, pH 7.4), and imaged in clean water medium using liquid-based atomic force microscopy (AFM) over 10 days. The size of oligomeric aggregates formed during the embryonic phase when the α-Syn solution was incubated for 10 days at 37 °C under constant mechanical agitation (see the

Received: January 8, 2022
Accepted: March 23, 2022
Published: April 12, 2022

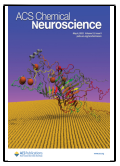

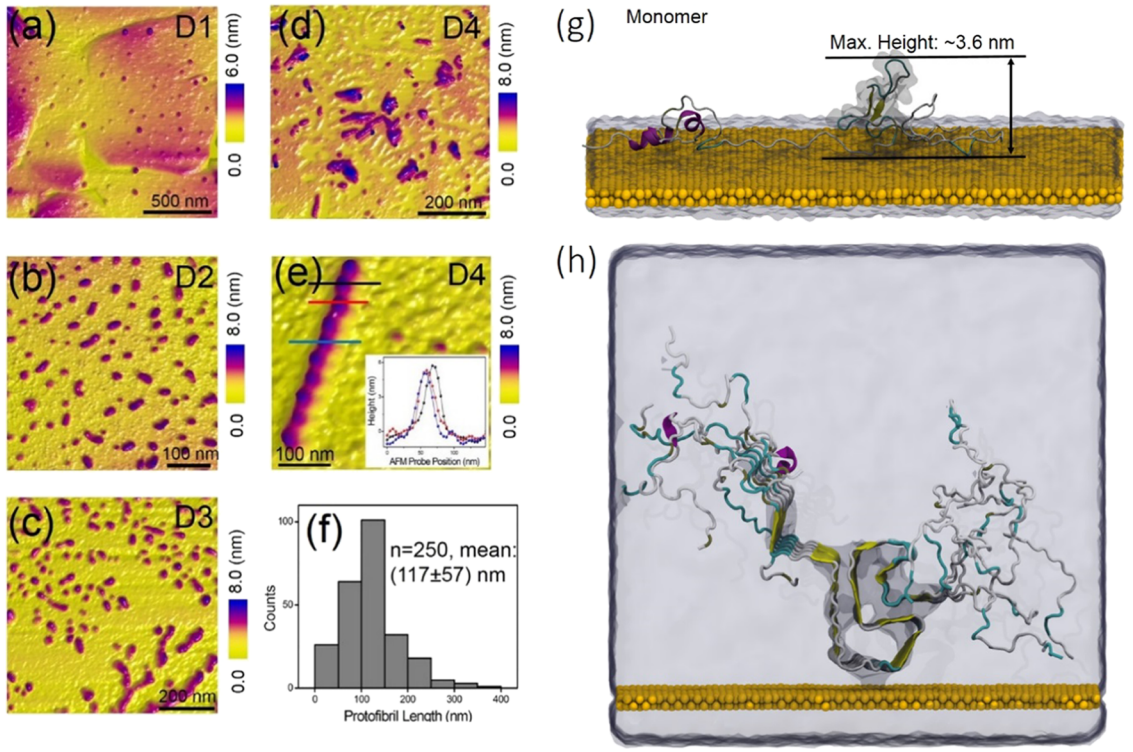

Figure 1. Embryonic and lag phase of α-Syn aggregation at the gold−water interface. (a) Large-area AFM topographic image of α-Syn peptides in the form of monomers and small oligomers adsorbed on the terraces of ultraflat gold (surface roughness of bare gold regions: ~0.2 nm). The AFM data shown in panels (a−d) were recorded after incubating the α-Syn solution at 37 °C under mechanical agitation for 1−4 days, respectively, as labeled D1−D4. Mostly large oligomeric particles were detected on day 2 of incubation (panel b), and oligomeric and dendritic α-Syn structures were observed on Au(111) after 3 days of incubation of the α-Syn solution (panel c). Protofibrillar structures were only observed after 4 days of incubation of the α-Syn solution (panel d). (e) Spatially well-resolved AFM image of a single protofibril revealing a nodular "beaded" architecture with 5−6 nm spherical particles (see measured heights in the inset) arranged in the form of a linear chain. (f) Statistical analysis of the protofibril length distribution after 4 days of α-Syn incubation. (g) Representative structure of α-Syn monomer showing its most stable maximum height on the Au(111) surface during 200 ns dynamics. The non-amyloid-β component (NAC; residues 61−95) region is shaded in gray. (h) α-Syn hexamer oriented on the surface of Au(111) (golden color) showing the full periodic solvated simulation cell.

Methods section) is resolved with single-particle resolution. The differences in onset time and size values of protofibrillar and mature fibrillar aggregates formed along the aggregation pathway in the three sets of conditions highlight the importance of using controls and repeat experiments to properly characterize the aggregates (discussed under Supporting Section S1). A distinct increase in fibril length was observed during the elongation phase. Moreover, gradual evolution of the fibrils from a two-dimensional (2-D) format to a three-dimensionally (3-D) packed arrangement was observed toward the saturation phase of α-Syn aggregation. Raman spectroscopy conducted on air-dried α-Syn aggregates formed during the 10 days of incubation revealed an increased intensity of the amide I band from *embryonic* (monomers and small-sized oligomers), *lag* (large-sized oligomers and short fibrils), and *elongation* (isolated and elongated fibrils) to *saturation* phase (dense mature fibrillar networks). Incubating α-Syn solution with copper metal ions resulted in accelerated α-Syn aggregation and the formation of annular oligomers at the embryonic phase, which was not detected when α-Syn was incubated in the absence of copper(II). Annular oligomers have been previously detected when α-Syn was incubated with calcium(II), which bound to the α-Syn C-terminal domain,[17] while Cu(II) binding to α-Syn single monomers was found to accelerate their self-assembly at physiologically relevant conditions[18−20] and mediate α-Syn oligomeric toxicity.[21,22]

The results from AFM obtained in the present study are complemented by molecular dynamics (MD) computer simulations of an experimental α-Syn protofibrillar structure at the gold−water interface. Modeling the α-Syn monomer, dimer, trimer, and hexamer superstructures identified in the experiments allows us to accurately map the dimensions, supramolecular packing interactions, and thermodynamic stabilities that direct the nascent stages of self-assembly and profibrillar elongation in copper-free conditions and in the presence of low and high concentrations of Cu(II) ions.

Overall, our experimental/modeling approach allows us to capture the changes in size, shape, and conformation of the α-Syn protein aggregates in response to perturbations in the chemical environment. By delineating the change in aggregation mediated by physiological concentrations of divalent metal Cu(II) ions, we show the potential of liquid-based AFM in studying protein aggregation at a solid−liquid interface.

RESULTS AND DISCUSSION

Embryonic and Lag Phase of α-Syn Proteins at the Gold−Water Interface. Figure 1a shows a large-area AFM image of α-Syn aggregates absorbed at the gold−water interface. The topographic map was captured immediately after deposition of α-Syn particles (which had been incubated for 1 day) in buffered aqueous solution followed by rinsing the

https://doi.org/10.1021/acschemneuro.2c00021
ACS Chem. Neurosci. 2022, 13, 1410−1421

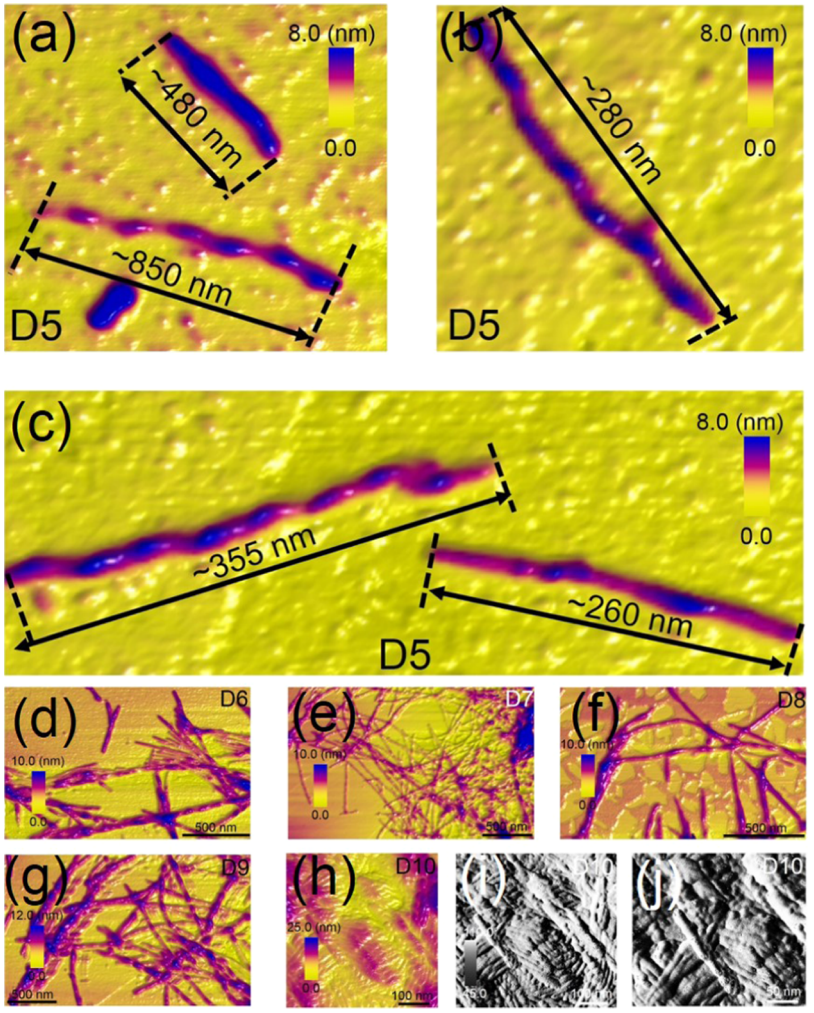

Figure 2. Elongation and saturation phase of α-Syn. (a–c) High-resolution AFM height images of mainly protofibrillar aggregates with typical nodular morphology observed on Au(111). The first onset of mature fibrillar aggregates (indicated by the black arrow in panel a) was only observed after the α-Syn solution was incubated for 5 days. Only a minor increase in fibril height was detected on day 5 compared to the fibril height measured on day 4 of α-Syn solution incubation. High-resolution AFM topographs revealing the evolution in spatial organization of fibrils from a sparse to dense network on gold after the α-Syn solution was incubated for 6 days (d), 7 days (e), 8 days (f), 9 days (g), and 10 days (h). The phase-contrast images (i, j) reveal the close-packed and layered arrangement of α-Syn mature fibrils on gold recorded on day 10 of the aggregation pathway of α-Syn proteins.

surface with clean water and continuing to image in water (see details under the Methods section). The simultaneously acquired phase-contrast image (see Supporting Information Figure S1) shows distinct differences in the particle sizes. Individual height profile traces measured over the particles numbered from I to VI on the phase-contrast image are plotted in Figure S1c–e, which reveals the exact differences in particle height relative to the underlying gold substrate. From the height profiles, the particle width appears larger than the true width due to AFM tip convolution effects. However, the height profile values are independent of tip effects, and as the height equals the diameter of a sphere, it is reasonable to estimate the diameters of α-Syn particles. After 1 day of incubation, only particles with diameters ranging from ~0.5 to ~7.5 nm were detected from the AFM measurements in a clean water medium. We calculated a mean diameter of 4.1 ± 3.6 nm for the single particles. Figure 1b is the AFM height image acquired after incubating α-Syn for 2 days. The individual height profiles obtained in clean water on day 2 (Figure S1) show a slight increase in particle diameter, ranging from ~1.5 to ~8.5 nm with a mean particle diameter of 5.0 ± 3.5 nm. AFM measurements conducted on day 3 revealed mainly dendritic aggregates together with single particles of varying sizes (Figure 1c).

Based on the AFM topographic images obtained on day 3 of α-Syn incubation, we calculate a mean particle diameter of 5.5 ± 2.2 nm averaged over height profile traces measured from approximately 500 particles. During the first 3 days of α-Syn incubation, only single spherical particles, jellybean-shaped particles, and dendritic structures were detected. Based on the evolution of particle size and shape, we classify this period as the *embryonic phase* of α-Syn aggregation. After 4 days of α-Syn incubation, fibrillar aggregates were detected on the gold surface, signaling the start of the *lag phase*. Figure 1d is a high-resolution AFM topograph of a region with predominantly fibrillar aggregates present together with a small population of spherical particles recorded on day 4 of α-Syn incubation. Closer inspection of the fibrillar aggregates revealed them to be protofibrillar strands with a typical nodular "beaded" type architecture,[23] as clearly seen in the AFM topograph (Figure

https://doi.org/10.1021/acschemneuro.2c00021
ACS Chem. Neurosci. 2022, 13, 1410–1421

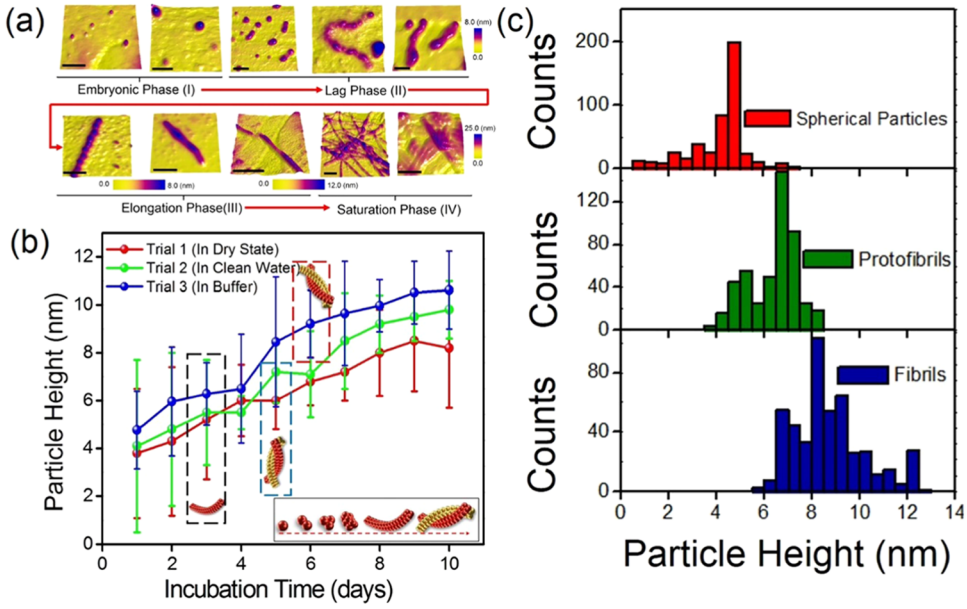

Figure 3. Full spectrum of α-Syn aggregate morphology from monomers to fibrils resolved on gold. (a) Overview of the α-Syn aggregation landscape with representative AFM images mapping the transition from the embryonic phase to lag, elongation, and saturation phase. The scale bar in all AFM images is 100 nm. (b) Plot of the increase in height values of the full spectrum of particles from monomers to fibrils measured as a function of α-Syn solution incubation time over a span of 10 days. The red, green, and blue plots correspond to particle heights measured separately in three different trials in a dry state, clean water, and in buffer medium, respectively, from n = 150 measurements recorded each day of each trial. Protofibrillar aggregates were first detected on the third day during all of the trials (marked by the black dashed box in panel b). The onset of mature fibrillar aggregates was observed only on the fifth day of α-Syn solution incubation during trials 1 and 2 (indicated by the blue dashed box in panel b) and was detected on the sixth day during trial 3 (indicated by the red dashed box in panel b), which was conducted in the buffer solution environment. (c) Statistical analysis of α-Syn aggregate height of all of the small spherical oligomeric (red histogram), protofibrillar (green histogram), and mature fibrillar (blue histogram) species measured from the AFM images recorded in clean water on gold (trial 2). The measured particle height equals particle diameter for the spherical and cylindrically shaped aggregates.

1e). Based on the sectional profile and fibril length analysis of approximately 250 single protofibrils from AFM topographs obtained in clean water, we calculate mean diameter and mean length of 5.5 ± 0.7 and 117 ± 57 nm (Figure 1f), respectively. The measured mean protofibril diameter from our study is consistent with previous AFM reports on α-Syn protofibril morphology.[23−25] To identify α-Syn monomers present within the lower bound of the size distribution of particles measured using AFM, we employ a previously reported protocol to convert measured aggregate volume to molecular weight[26] by assuming a spherical shape for the single α-Syn particles. Based on this assumption, we estimate that the α-Syn particles with a height profile of ∼3 nm correspond to a molecular weight of ∼14.0 kDa, which is the known molecular weight of α-Syn monomer and comparable to previous AFM-based reports on α-Syn monomers.[27] This measured monomeric height profile is in close agreement with the α-Syn monomer height distribution predicted from the MD simulations (typical structure shown in Figure 1g, data discussed below).

Quantifying the Elongation and Saturation Phase of α-Syn Proteins. Upon registering the onset of short protofibrils on day 4 of α-Syn incubation and resolving their morphology, the formation of elongated fibrils was first observed after 5 days of incubation, which we identify as the elongation phase. Figure 2a−c shows high-resolution AFM height images showing the presence of elongated fibrils at the gold−water interface and highlighting differences in fibril length. Although the fibrils appear elongated, the beaded morphology is still clearly visible from the AFM images (Figure 2c). In addition to the formation of elongated fibrils, there was a significant reduction in the population of oligomeric aggregates on the gold surface in the AFM images obtained on day 5 of α-Syn incubation, indicating the near-complete conversion of oligomeric to fibrillar aggregates. However, only a marginal increase in the height of the fibrils was measured (Figure 2a−c), which indicates that α-Syn elongation to mature fibrils might occur in a single layer as opposed to the stacked Amyloid-β aggregation imaged at a graphene−water interface,[28] reflecting the longer, heavier α-Syn compared to amyloid-β proteins (molecular weight: ∼4.5 kDa).

The evolution of α-Syn assembly transits from embryonic, lag, and elongation phase by interconverting between a series of transient nanostructures from monomers, small and larger-sized oligomers, short protofibrils, and elongated protofibrils, as recorded using AFM from day 1 to day 5 of incubation. From day 6 onwards, we observed a gradual increase in fibril length and conversion of protofibrils into mature elongated fibrils, as marked by the absence of beaded morphology in Figure 2d. Figure 2e−g shows high-resolution AFM height images that capture the transition from very sparse to more closely packed 2-D fibrillar networks between day 7 and day 9 of α-Syn solution incubation. The 2-D fibril networks expanded into a dense 3-D network composed of closely packed and intertwined fibrils on day 10 of α-Syn incubation, as shown in the AFM height (Figure 2h) and phase-contrast images (Figure 2i,j). The height profiles extracted along the fibril networks (see Figure S2) quantify the increase in fibril height with time. Importantly, beyond these 10 days we did not observe any further changes in fibril morphology or packing order during a further 5 days of monitoring. Hence, we

https://doi.org/10.1021/acschemneuro.2c00021
ACS Chem. Neurosci. 2022, 13, 1410−1421

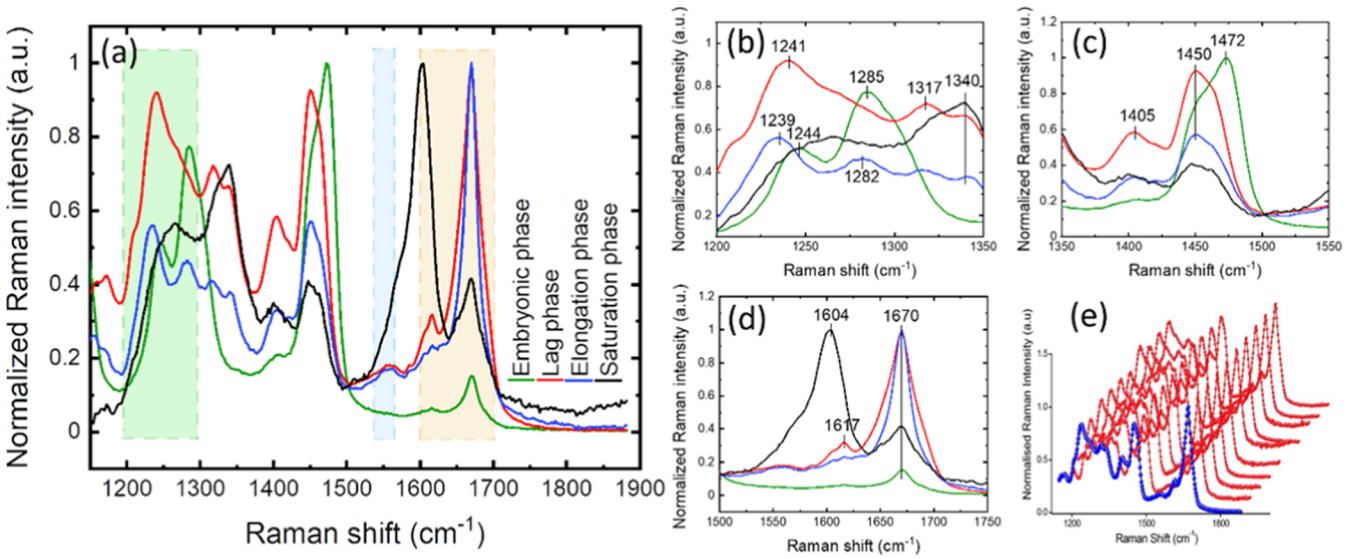

Figure 4. Spectrochemical analysis of α-Syn aggregation phases. (a) Averaged spectral signature of the aggregates recorded during the embryonic phase (green plot), lag phase (red plot), elongation phase (blue plot), and saturation phase (black plot). (b) Amide(III) spectral region (1200−1300 cm^{-1}) indicated by the green shaded region in panel (a). (c) Close up of the central region (1350−1550 cm^{-1}) including the amide(II) spectral region (1500−1550 cm^{-1}) indicated by the blue shaded region in panel (a). (d) Amide(I) spectral region (1600−1700 cm^{-1}) indicated by the orange shaded region in panel (a). (e) Individual spectroscopic traces (shown in red plot), and the averaged spectral plot (shown in blue plot) acquired during the elongation phase of α-Syn aggregation.

identify this period from day 6 to 10 as the *saturation phase* of α-Syn aggregation.

Figure 3a is a summary of representative AFM images recorded over the 10 day α-Syn incubation period starting from the embryonic phase with predominantly monomers and small oligomers, followed by a lag phase with larger-sized oligomers and dendritic structures to an elongation phase with the first occurrence of short protofibril, and finally the saturation phase with mature fibrillar networks. All AFM images shown in Figure 3a were recorded at the gold−water interface. The quantitative analysis of the α-Syn aggregation pathway (Figure 3b) shows the increase in particle height over time for measurements conducted in the dry state (red trace), clean water (green trace), and in buffered salt solution (blue trace). Protofibrillar aggregates were first detected on day 3 during all of the trials (black dashed box in Figure 3b). The onset of mature fibrillar aggregates was observed only on day 5 of α-Syn solution incubation during trials 1 and 2 (blue dashed box in panel b) and was detected on day 6 during trial 3 (red dashed box in panel b), which was conducted in buffer. Figure 3c is a comprehensive statistical analysis of α-Syn aggregate height of all particles detected in the AFM images recorded in clean water on gold (trial 2), ranging from monomers and small spherical oligomers (red histogram) to protofibrils (green histogram) and mature fibrils (blue histogram). From the statistical distribution, we calculate a mean spherical particle diameter of 4.0 nm with a confidence interval lower (CIL) of 3.9 nm and a confidence interval upper (CIU) of 4.15 nm. Next, we calculate a mean protofibril diameter of 6.1 nm with a CIL of 6.05 nm and a CIU of 6.25 nm. Finally, we calculate a mean mature fibrillar diameter of 8.5 nm with a CIL of 8.40 nm and a CIU of 8.67 nm. The confidence interval (CI) was calculated at 95% statistical distribution as the plots shown in Figure 3c is non-Gaussian. In general, the findings from our study on the size, shape, and morphology of the α-Syn protein aggregates formed at different points along the aggregation pathway are consistent with previous imaging studies of α-Syn aggregation.[23−25,27,29−33] Our comparative study highlights that the exact onset time of protofibrils and fibrils will depend on multiple factors, such as the α-Syn solution concentration, as well as its purity, preparation, and mixing conditions. For example, we conducted parallel measurements on α-Syn solution that was not mechanically agitated at 37 °C. It was only after nearly 6 months that we were first able to observe α-Syn mature fibrillar networks on gold similar in topology to the data shown in Figure 2g,h.

Spectrochemical Profile of α-Syn Protein Aggregation Pathway. To chemically characterize the ensemble of aggregated states occurring along the α-Syn assembly pathway, we conducted Raman spectroscopy measurements (see the Methods section). Figure 4a shows Raman spectra of α-Syn aggregates measured in the four phases identified by AFM analysis. The morphology of the diverse α-Syn aggregates in these respective phases is shown in Figure 3a, and their sizes are quantified in Figure 3b,c. In the amide(III) region (resulting from C−N stretch and N−H bend vibrations) (Figure 4b), a shift to the left of a peak maximum can be observed that corresponds to the β-sheet content, in the region from 1220 to 1248 cm^{-1}.[34] The peak maximum in the embryonic phase is located at 1244 cm^{-1}, while in the lag phase, it is at 1241 cm^{-1}, and in the elongation phase at 1239 cm^{-1}. The shift of this peak corroborates spectra obtained by Flynn et al.[29] in earlier studies of α-Syn aggregates. Interestingly, we also observe a shift of a secondary peak from 1285 to 1282 cm^{-1} from the lag to elongation phase, which indicates a potential decrease in α-helical content. Along with the increase in β-sheet content, this shift further highlights aggregation as previously proposed by Apetri et al.[30] Spectral bands at 1405 and 1450 cm^{-1} (Figure 4c) mainly appear due to the side-chain vibrations, such as CO^{2-} (1405 cm^{-1}, symmetric stretch) and CH_2, CH_3 deformations (1450 cm^{-1}).[35] These bands are present in the observed spectra throughout the aggregation process. For the lag and elongation

https://doi.org/10.1021/acschemneuro.2c00021
ACS Chem. Neurosci. 2022, 13, 1410−1421

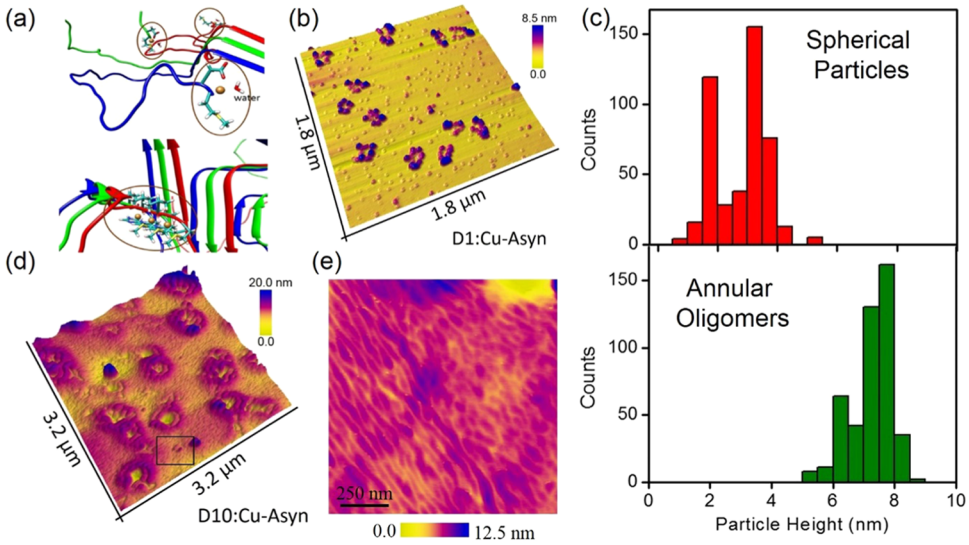

Figure 5. Cu^{2+} induced annular oligomers and accelerated α-Syn aggregation. (a) N-termini of three monomers of α-Syn trimer showing the [PDB code: 2N0A] coordination of Cu^{2+} (circled in red) with residues Met1, Asp2, and a water molecule with a Cu^{2+}/monomer ratio of 1:1. (b) 3-D represented the AFM image of annular-shaped oligomeric α-Syn aggregates resolved at the gold−water interface after incubating the α-Syn solution with copper for 1 day. In addition to the annular oligomers, spherical particles with varying sizes are also visible from the AFM topograph. (c) Statistical analysis of the size distribution of spherical particles (red histogram) and annular-shaped oligomeric particles (green histogram). From the statistical plot, we calculate a mean particle size of 2.6 ± 0.8 nm for the spherical particles and 7.1 ± 0.7 nm for the annular-shaped α-Syn oligomers. (d) 3-D represented AFM image of a dense and multilayered film composed of α-Syn fibrillar resolved at the gold−water interface after incubating the α-Syn solution with Cu for a period of 10 days. (e) AFM height image recorded within the black rectangle region indicated in panel (d), showing closely packed fibrillar aggregates.

phases, we observe a low-intensity peak around ∼1550 cm^{-1}, which is the expected region of the amide(II) band.

Additionally, in the amide(I) region (mostly due to C═O stretching), shown in Figure 4d, an increase in the intensity of the peak at 1670 cm^{-1} was detected compared to the intensities of the peaks in the amide(III) region, during aggregation from the embryonic to elongation phase. This specific peak is indicative of β-sheet structure and content[34] and shows similar β-sheet content between lag and elongation phases. For the spectra recorded during the saturation phase (shown in Figure 4a), a peak with a maximum at 1670 cm^{-1} is less prominent. In this phase, a strong peak with a maximum at 1604 cm^{-1} was observed, which was not present in the previous aggregation states. This peak could be attributed to Phe,[35] but it is usually weak.[30] Therefore, a more likely assignment of the peak at 1604 cm^{-1} is a shift of amide(I) band upon aggregation.

Such difference in the spectra, in comparison to the previous phases, indicates that major changes occur in the overall structure of ensemble of α-Syn aggregates from oligomers to mature fibrils. Finally, Figure 4e shows the close matching between Raman spectra acquired during the elongation phase (in red) in the different areas on the sample and the averaged spectra (in blue), illustrating the robustness of the method. In general, the Raman spectroscopy measurements acquired over large-area spanning diverse ensemble of aggregates substantiate the high-resolution AFM data obtained at a single-particle level on the presence of higher-order α-Syn protein aggregates with increasing α-Syn solution incubation time.

Copper-Modulated Aggregation Pathway of α-Syn Proteins. Upon clarifying the morphological and chemical profile of the α-Syn aggregation pathway at the gold−water interface, we investigated the specific effect of copper(II) on α-Syn aggregation. The 10 day incubation was repeated in the presence of Cu^{2+} (see the Methods section), with the Cu^{2+}-containing α-Syn solution drop-casted on gold and the measurements conducted in buffer salt solutions to first check the nature of the aggregates before rinsing them with clean water for more accurate profiling of α-Syn aggregate size and shape. The Cu^{2+}−α-Syn complex is shown in Figure 5a.

The key finding during our AFM measurements when analyzing the α-Syn solution incubated with Cu^{2+} for 1 day was the observation of annular oligomeric structures (Figure 5b), which we did not observe when only α-Syn was incubated under the same conditions of 37 °C and mechanical agitation. Although the annular oligomers were the most abundant species distributed on the gold surface, spherical aggregates were also present, as seen from the AFM image (Figure 5b). Moreover, a low population of sparsely distributed archetypal α-Syn protofibrils was observed. Upon measuring the size distribution of annular oligomeric (green histogram, Figure 5c) and spherical aggregates (red histogram, Figure 5c) from the AFM height maps, we calculate a mean particle size of 2.63 nm (CIL: 2.55 nm and CIU: 2.7 nm, CI at 95% statistical distribution) for the spherical particles, which is smaller than the mean particle size observed for Cu^{2+}-free α-Syn spherical particles of 4.0 ± 1.2 nm, possibly reflecting bridging of charged groups by the metal ions to create more compact monomers (described in the MD models in the next section). By contrast, the mean size of the annular-shaped α-Syn oligomers was estimated to be 7.03 nm (CIL: 6.95 and CIU: 7.10 nm, CI at 95% statistical distribution).

Finally, from the height profiles of the few protofibrils in the presence of Cu(II) (see Figure S5), we calculate a mean size of 5.8 ± 0.8 nm. Furthermore, the addition of Cu^{2+} resulted in a dramatic acceleration of aggregation time scales evidenced by the early formation of fibrillar aggregates after just 2 days of incubation (Figure S5). These findings indicate that incubating

https://doi.org/10.1021/acschemneuro.2c00021
ACS Chem. Neurosci. 2022, 13, 1410−1421

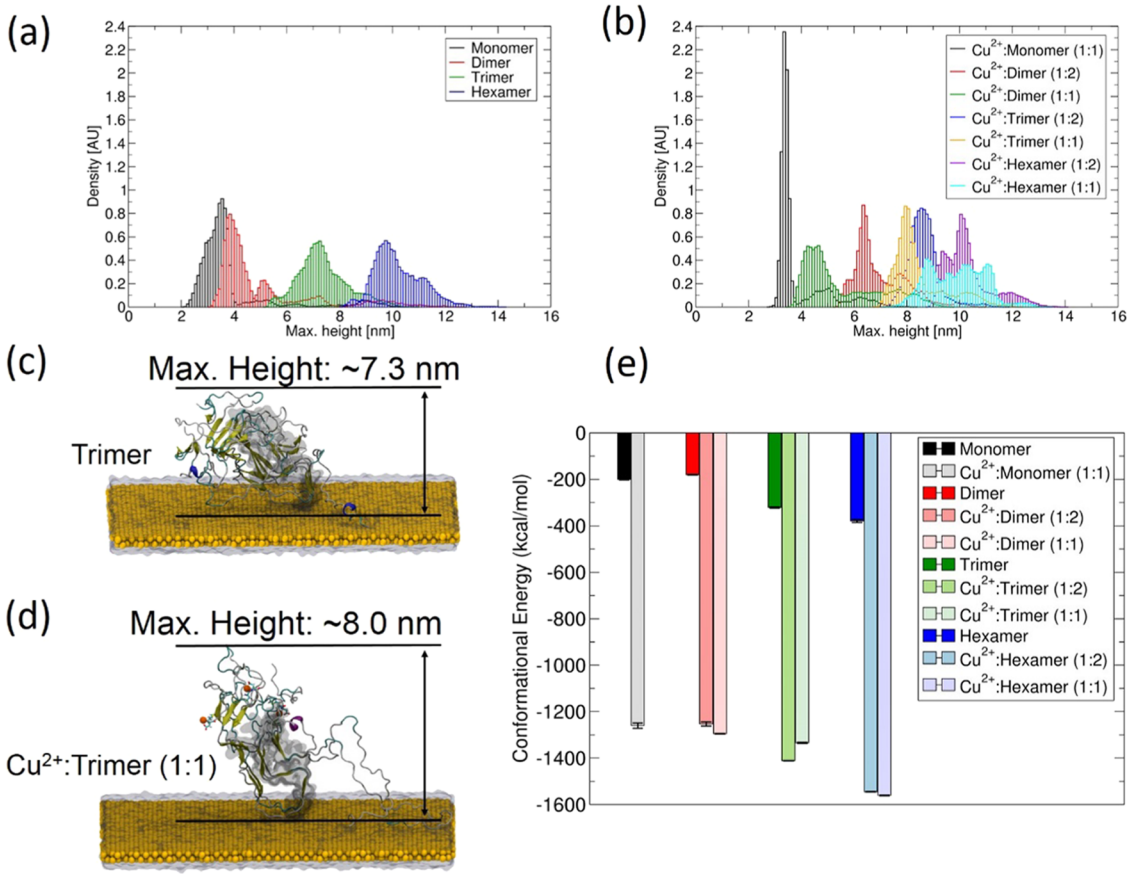

Figure 6. MD simulation of Cu^{2+} effects on α-Syn oligomers. (a) Computed distribution of monomer and oligomer maximum heights on the surface of Au(111), with height populations counted as densities with arbitrary units. (b) Computed distribution of monomer and oligomer maximum heights in complex with Cu^{2+} at two different Cu^{2+}/assembly ratios (1:2) and (1:1) on the surface of Au(111). (c) Representative structure of α-Syn trimer showing typical maximum height on the Au(111) surface during 200 ns dynamics. (d) Representative structure of α-Syn Cu^{2+}/trimer (1:1) showing typical maximum height on the Au(111) surface. (e) Mean conformational energies of monomer and oligomers (normalized per monomer) during the final 50 ns of molecular dynamics.

α-Syn with Cu^{2+} selectively induces the formation of annular oligomers and also accelerates the transition of α-Syn from monomeric to fibrillar forms. Figure 5d is an AFM image showing a dense and multilayered film composed of α-Syn fibrils resolved at the gold−water interface after incubating the α-Syn solution with Cu^{2+} for a period of 10 days (see Figure S6). A spatially magnified AFM image is shown in Figure 5e recorded within the region indicated by the black rectangle in Figure 5d, showing clearly the presence of elongated fibrils. Although the acceleration of α-Syn aggregation when exposed to Cu^{2+} is known from previous studies[18,36,37] and the formation of annular-shaped α-Syn oligomers has been detected in the presence of calcium(II) ions,[17] the current study provides real-space evidence for Cu^{2+}-associated annular oligomers with single-particle level specificity.

Molecular Simulations of α-Syn Monomer and Oligomers at the Gold−Water Interface. To gain a deeper understanding of Cu(II)-mediated α-Syn assembly from monomers to higher-order oligomers at the gold−water interface, we performed a total of 2.4 ms of room temperature molecular dynamics in water. We calculated the structure, dynamics, and energetics of four different α-Syn species with no, low, and high levels of Cu(II) during 0.2 μs of dynamics for each, modeling Cu^{2+}-free monomer, dimer, trimer, and hexamer starting from their protofibrillar folds[38] and of the assemblies forming coordination complexes with Cu^{2+} at two different Cu^{2+}/α-Syn ratios (1:2 and 1:1) to closely mimic the sub-μM and μM Cu^{2+} concentrations used in the experiments (see Figure S7 and the Methods section). The overall α-Syn dimensions (radius of gyration, R_g) of our well-converged models (see RMSD plots in Figure S9a,b) track the growth of the α-Syn assembly as monomers are added (see Figures S8a−k and S9c,d). Notably, the structures become more elongated and more extended in the presence of Cu^{2+} (Figure S9d), except for monomer, where Cu^{2+} mediates significant NT−CT interactions (Figure S10b) and also direct CT−Cu^{2+} (Figure S12a) interactions. At high Cu^{2+} concentrations (1:1), dimer and hexamer are more compact than at low concentrations of Cu^{2+} (1:2), while the opposite effect is observed for trimers (see Figure S9c,d). An overall globular shape (Figure S9e,f) is predicted for all assemblies with the monomer (without Cu^{2+}) displaying a rodlike morphology (Figure S9e). Interestingly, the mean oligomeric length profile (Figure S9) tracks the distortion of the dimer model in the absence of Cu^{2+} and the compaction of dimer and hexamer in the presence of Cu^{2+} (Figure S9i,j).

Since the sampled sizes in our models predict the protein heights on the gold Au(111) surface, we evaluate the maximum height profiles and compare our findings with the AFM experiments. For all systems, we observe an initial

https://doi.org/10.1021/acschemneuro.2c00021
ACS Chem. Neurosci. 2022, 13, 1410−1421

collapse of the assemblies at the gold−water interface, which are most obvious for monomers and dimers (Figure S9g,h). Figure 1g shows the α-Syn monomer at the gold−water interface with a typical height of ∼3.6 nm (Figure 6a), which is consistent with the experimentally estimated height value of ∼3 nm. The computed α-Syn monomer dynamics shows the formation of α-helices in the N-terminus with a β-hairpin formed close to the NAC region. Recent studies on monomers and dimers have indicated that α-Syn samples a heterogeneous ensemble of interconverting conformations in an aqueous solution, including parallel and antiparallel β-sheets and transient α-helical conformations,[27,39−42] with long stretches of α-helices predicted to impede pathogenic aggregation of α-Syn.[43−45] However, compared to α-Syn in bulk water, the reduced conformational freedom of α-Syn at the gold−water interface may stabilize fibril-like morphologies, as also noted previously for adsorption of amyloid-β-42 peptide on gold[46] and amyloid-β-42 protofibrils on graphene.[28] For the Cu^{2+}/monomer (1:1) complex, the maximum height is ∼3.4 nm with a narrow distribution showing that the high affinity of Cu^{2+} for NT compacts the monomer (Figure 6b) *via* additional Cu^{2+}−CT interactions (Figure S12a) and is close to the maximum height of spherical particles when exposed to 1 μM Cu^{2+} obtained from our AFM experiments (∼3.25 nm) (see Figure 5c, red histogram). The Cu^{2+}−CT interactions are also prevalent for hexamers and proportional to the copper concentrations used (Figure S12f,g), sampling more collapsed conformations (∼8.8 nm maximum height) at higher 1:1 Cu^{2+} concentration than at lower 1:2 concentration (∼10.1 nm maximum height) (Figure 6b) and in the absence of Cu^{2+} (∼9.8 nm height; see Figure 6a). By contrast, for dimers and trimers Cu^{2+} stabilizes taller assemblies (Figure 6a,b) that are less collapsed than without the Cu^{2+} (Figure S9g,h), reflecting the large dependence of Cu^{2+} structure-directing effect on the size and state of the assembly.[47] For all oligomer constructs, at full μM concentrations of Cu^{2+}, we observe more collapsed, shorter assemblies than at sub-μM concentrations (Figure 6b).

Our α-Syn dimer model (without Cu^{2+}) with a peak height of ∼3.9 nm (Figure 6a) matches the mean height of small spherical particles (∼4 nm) estimated from AFM statistical analyses of α-Syn aggregates (see Figure 3c), identifying these observed assemblies as possible dimers and the most abundant nonmonomeric spherical oligomers without copper. The measured particle height (∼7 nm from the peak in the histogram) in the protofibrillar fold (Figure 3c) closely matches the trimer height peak maximum height of ∼7.3 nm (Figure 6c) in our predictive models, which indicates that trimers may be critical for elongation in the absence of Cu^{2+}. By contrast, the majority of the spherical particles measured in the presence of Cu^{2+} (see Figure 5c, red histogram) are of dimension similar to the height of monomers (∼3.4 nm) in our simulations (Figure 6b), and smaller than the dimer heights (∼3.9 nm) predicted in the absence of Cu^{2+} (Figure 6a) and estimated from AFM experiments (see Figure 3c).

The Cu-free α-Syn trimer is a stable protofibrillar oligomer assembly (see Figure 6e), stabilized by a E46−K80 salt bridge (Figure S13a) and a strong hydrogen bond (H-bond) network (Figure S14a,e), and displays the highest content of β-sheet (Figure S13b) among all constructs. Taking into account also the approximately doubled likelihood to form the hexamer than elongate from the dimer (from the predicted conformational energies in Figures 6e and S13d), we propose that the minimal critical protofibrillar nucleus for α-Syn growth is formed by the trimer (Figure 6c). The Cu^{2+}-bound complexes are massively stabilized relative to the assemblies without Cu^{2+} (Figure 6e). We predict that Cu^{2+}−trimer complexes at a lower concentration of Cu^{2+} (1:2 ratio) may be the minimal oligomeric fragment in protofibrillar fold capable of further lateral elongation given their very stable E46−K80 salt bridge (which is unstable up to dimer; see Figure S13a) and retention of high percentage of residues in β-sheet, which makes them more structured than the Cu^{2+}−hexamer complexes (see Figure S13c). The protofibrils were detected to be low in distribution at high experimental Cu^{2+} concentrations (1 μM) used in AFM measurements but may be stabilized at low (sub-μM) Cu^{2+} concentrations as predicted from our MD model of the trimer−Cu^{2+} complex.

We also note from Figure 5c (green histogram) that the major population (from the peak of the distribution) of annular oligomers with Cu^{2+} estimated at a height of 7.75 nm is closer to our most populated height of the Cu^{2+}/trimer (1:1) model (∼8 nm) than the Cu^{2+}/Trimer (1:2) model (∼8.6 nm) (Figure 6b−d). This may be explained by the model-predicted destabilization of the trimer in the protofibrillar fold at the higher concentration of Cu^{2+} (Figures 6e and S13c−e). Previous reports have suggested that annular protofibrils are known to nucleate α-Syn filament formation and are cytotoxic,[17] and that the morphology of porelike annular oligomers can vary between different architectures.[48] Several groups have also identified pore-forming annular α-Syn protofibrillar oligomers with high content of β-sheet[49,50] or antiparallel β-sheet[51] with excellent seeding capabilities. Our Cu^{2+}/trimer (1:1) model with a Greek-key core may represent the precursor to these ringlike architectures of polymorphic annular protofibrils (cross-β sheet *vs* β-barrel, respectively). The predicted instability of trimers at high Cu^{2+} concentration (Figure 6e; all other assembly constructs are more stable at higher Cu^{2+} concentration) may facilitate conformational rearrangements to a metastable, amorphous state at longer time scales, consistent with the assembly of looser-packed, more porelike annular architecture, minimally formed by the trimers.[52] At lower Cu^{2+} concentration, the higher stability of trimers (Figures 6e and S13e; also evident from the intermonomer H-bonds in Figure S14f,g) may be capable of seeding fibril growth *via* lateral monomeric interactions to create an elongated linear chain of fibrils along the gold surface.

In summary, our AFM experiments clearly identify annular oligomers as the dominant species at 1 μM copper(II) concentration, which could potentially be formed by Cu^{2+}/trimer (1:1) from our MD models, while we rationalize that at sub-μM copper(II) concentrations, the Cu^{2+}/trimer (1:2) model may retain the profibrillar morphology to initiate fibril growth, which are the sparsely populated species observed in the AFM images. More details of the above analyses are provided in Section 2.5 Supporting Analyses.

DISCUSSION

Here, we combine nanoscale imaging, chemical spectroscopy, and atomic-scale modeling to construct a detailed picture of the assembly of α-Syn proteins in the presence and absence of Cu(II) ions. The AFM results highlight the importance of registering the size and shape evolution of α-Syn protein aggregates when retaining them in a hydrated state. Raman spectroscopy-based analysis of α-Syn aggregated states reveals information on the increase in β-sheet content during the

https://doi.org/10.1021/acschemneuro.2c00021
ACS Chem. Neurosci. 2022, 13, 1410−1421

elongation phase and decrease in α-helical content observed for the lag and elongation phases through analysis of the amide bands. Atomic-scale molecular dynamics (MD) models predict the early stages of self-assembly, allowing us to identify the likely structures in our AFM height profile maps. Our models reveal that the minimal critical nucleus necessary for elongation of the α-Syn protofibrillar fold is a trimer as estimated from the AFM height profiles on gold. This is in agreement with recent studies of α-Syn in Greek-key fold,[53] while the spherical particle observed in the AFM measurements corresponds to a monomer or dimer. We confirm that the size of α-Syn monomer from our model is in good agreement with the size estimated from the AFM data obtained when the proteins were retained in a hydrated interface. The α-Syn assemblies are very effectively sealed and reinforced by binding to copper(II) with the AFM-measured heights of the densely populated spherical particles observed in the presence of copper closely corresponding to a Cu^{2+}-bound monomer computed from our MD models.

Strikingly, the binding of trimer to a high concentration of Cu^{2+} renders them more thermodynamically unstable than at low Cu^{2+} concentration (opposite effect observed for all other assembly constructs), where the cross-β protofibrillar fold is retained to a greater extent. Previous studies have identified a dynamic, interconverting population of different oligomeric morphologies in α-Syn self-assembly.[51,54,55] Among these, the protofibrillar (chainlike) and annular oligomers are known to be cytotoxic species,[17] the second category is further classified according to their architecture.[48,50] By cross-referencing our measured and model data, we predict Cu^{2+} concentration-dependent shape and thermodynamic signatures in trimers that may sufficiently distinguish α-Syn trimers as a critical-sized oligomer to form either chainlike or annular protofibrils. At low Cu^{2+} concentration, a more stable trimer may elongate the chain by addition of monomers laterally, while at high experimental Cu^{2+} concentration, the loss of stability could lead to conformational rearrangements leading to the formation of the annular oligomers with ringlike morphology detected in our AFM experiments after incubation with 1 μM concentration of copper(II). Recently, protein aggregates with protofibrillar and irregular annular oligomeric shapes with comparable size profiles, as reported in the present study, have been resolved and quantified on the surface of red blood cells from individuals with AD pathologies.[56]

The results from the present study highlight the importance of recording the morphological changes of pathological protein aggregates in response to their chemical environment. Such information obtained in the near native state of the protein aggregates could potentially serve as guidelines for better understanding protein aggregated states in body fluids from individuals who have been exposed to environmental metals over their lifetime. The nanoscale imaging, chemical spectroscopy, and integrated modeling-measurement methodologies presented here may inform rapid screening of other potential blood-borne cofactors, *e.g.*, other biometals, heavy metals, physiological amino acids, and metabolites, in directing and potentially rerouting IDP aggregation in the initiation and pathology of neurodegenerative diseases.

METHODS

Preparation of Wild-Type α-Syn Solution. Wild-type α-Syn was obtained by expression and purification in bacteria, as detailed by Campioni et al.[57] α-Syn solutions were prepared by dissolving the lyophilized protein (~30 mg/mL) in 2 mL of PBS buffer, pH 7.4. The solution pH was adjusted to 7.4 by adding 1 M NaOH (25−30 μL). The filter membrane of Amicon Ultra-4 Centrifugal Filter Unit (NMWL 100 kDa) was first hydrated in the centrifuge three times with 4 mL of PBS buffer (3200*g*, 5 min), followed by centrifugation of α-Syn solution (typically 2 mL) for 30 min to filter out large α-Syn particle chunks that were not fully dissolved. Two hundred microliters (or 10% of solution volume) of PBS was added to the filter and mixed using a pipette to extract the remaining α-Syn from the bottom of the filter, followed by centrifugation for 5 min. The final concentration of α-Syn (ε_{280} = 5960 M^{-1} cm^{-1}) was measured with spectrophotometer Implen Nanophotometer NP80 UV−vis. The solution was then diluted with PBS buffer to 300 μM α-Syn. V-shaped 1.5 mL protein LoBind tubes were filled with 500 μL of α-Syn solution and incubated in Eppendorf ThermoMixer C at 37 °C for 10 days under mechanical agitation at 500 rpm. To investigate the effect of Cu^{2+} ions on the α-Syn aggregation rate, its solution was added to the aliquot with α-Syn before the incubation. For each experiment, three aliquots of 300 μM α-Syn concentration were prepared for comparison. Cu^{2+} solution (10 μM) was prepared by dissolving copper(II) chloride in PBS buffer, pH 7.4 (Merck Millipore). Fifty microliters of prepared copper chloride solution was then added to the aliquot with 500 μL of α-Syn, leading to the final Cu^{2+} concentration of 1 μM.

Liquid-Based Atomic Force Microscopy. Liquid-based AFM was performed using a Multimode 8 AFM (Bruker) equipped with a liquid cell holder. A SCOUT 70 HAR silicon AFM tip with a high aspect ratio was used in tapping mode (gold reflective backside coating, force constant 2 N/m, resonant frequency: 70 kHz, NuNano). The AFM tip was cleaned by rinsing in acetone for 30 s and in isopropanol for ~1 min, followed by blow-drying with compressed air. After mounting the AFM tip in the tip holder, 5 μL of α-Syn in buffer salt solution was deposited on the Au(111) substrate. Before deposition of the α-Syn solution, Au(111) thin film on mica (purchased from Phasis, Inc) samples were thoroughly cleaned (rinsed with acetone and isopropanol, followed by blow-drying with N_2) and the surface quality of the gold thin film was checked using AFM. After ~2 min, the gold surface was gently flushed with 1 mL of pure water and the AFM tip was fully immersed and tuned in the water medium. For comparison, AFM measurements were conducted on α-Syn particles on gold substrates in buffer salt solution environment (5 μL), in clean water medium (5 μL), and also on air-dried samples (after removal of buffer salt solution with clean water). The standard deviations of particle heights of oligomers and fibrillar aggregates were calculated from measurements performed with 10 AFM tips of the same batch purchased from NuNano.

Raman Spectroscopy Setup and Measurements. Raman spectra were obtained using a WITec Alpha 300 R confocal Raman microscope. A 532 nm laser, spectrometer grating of 600 g/mm and Zeiss 100× objective, numerical aperture NA = 0.9 was used to acquire Raman maps (15 μm × 15 μm surface area, 1 μm step, 1 s integration time, 225 spectra in total) as well as time series (same spot, 60 spectra, 1 s integration time). Laser power was adjusted for different substrates: 40 mW for mica, 20 mW for silicon, and 10 mW for gold/mica. For every area scan, one average spectrum was obtained. To obtain representative spectra of the measured sample, average spectra of multiple areas were normalized and then averaged. Normalized spectra of different area scans were then averaged to obtain one representative spectra per sample. To compare the intensities of the peaks among different spectra, we normalized them to the Phenylalanine (Phe) band at 1003 cm^{-1} (Figure S3) as this band is less sensitive to the conformational changes of α-Syn proteins.[29] The background subtraction analysis is provided in Figure S4. Raman spectroscopy was conducted only on air-dried α-Syn (after removal of buffer salt solution with clean water) particles deposited on gold and also on mica substrates for comparison.

Molecular Simulations. The full details of model preparation, MD simulations, data analyses, and supplementary analyses are given in Supporting Section S2. Briefly, the starting models of free monomer and oligomers in Greek-key[38] fold α-Syn fibril structure were oriented with the fibril axis parallel to the gold Au(111) surface

https://doi.org/10.1021/acschemneuro.2c00021
ACS Chem. Neurosci. 2022, 13, 1410−1421

in a large periodic water-filled box (see Figures 1h and S7c–f). This starting orientation of α-Syn placed the NAC region in the Greek-key fold close to the gold surface. The models for Cu^{2+}-bound α-Syn constructs having the protofibrillar Greek-key fold[38] were generated from density functional theory (DFT) computed structures of the high-affinity Cu^{2+}-binding site in the N-terminus of α-Syn monomer obtained from a recent study,[47] showing Cu^{2+} coordinated to Met1, Asp2, and an ordered water molecule[58] (see Figures 5a and S7g; details in Section S2.1). To correspond closely with the final experimental Cu^{2+} concentration of 1 μM, we built the models of Cu^{2+}-bound α-Syn monomers and oligomers with Cu^{2+}/monomer ratios of 1:1 and 1:2 to observe the effect of varying copper concentrations at sub-μM copper(II) concentrations (see Figure S7h–n).

■ ASSOCIATED CONTENT

Supporting Information

The Supporting Information is available free of charge at https://pubs.acs.org/doi/10.1021/acschemneuro.2c00021.

Liquid-AFM-based analysis of α-Syn aggregate morphology; Raman spectroscopy measurements and details on molecular dynamics simulation of α-Syn aggregates in the presence and absence of copper ions (PDF)

■ AUTHOR INFORMATION

Corresponding Authors

Damien Thompson − *Department of Physics, Bernal Institute, University of Limerick, Limerick V94T9PX, Ireland;* orcid.org/0000-0003-2340-5441; Email: damien.thompson@ul.ie

Peter Niraj Nirmalraj − *Transport at Nanoscale Interfaces Laboratory, Swiss Federal Laboratories for Materials Science and Technology, Dübendorf CH-8600, Switzerland;* orcid.org/0000-0002-2282-6781; Email: peter.nirmalraj@empa.ch

Authors

Olena Synhaivska − *Transport at Nanoscale Interfaces Laboratory, Swiss Federal Laboratories for Materials Science and Technology, Dübendorf CH-8600, Switzerland*

Shayon Bhattacharya − *Department of Physics, Bernal Institute, University of Limerick, Limerick V94T9PX, Ireland;* orcid.org/0000-0002-4218-0308

Silvia Campioni − *Functional Materials Laboratory, Swiss Federal Laboratories for Materials Science and Technology, Dübendorf CH-8600, Switzerland*

Complete contact information is available at: https://pubs.acs.org/10.1021/acschemneuro.2c00021

Author Contributions

P.N.N. conceived the AFM and Raman spectroscopy study and performed the AFM measurements and data analysis. O.S. and S.C. prepared the α-Syn solutions. O.S. conducted the Raman spectroscopy measurements, data analysis, and Cu incubation of α-Syn solution. S.B. and D.T. conducted the molecular dynamics study and analyzed the simulation results. O.S., S.B., D.T., and P.N.N. wrote the manuscript. All authors discussed the results and commented on the manuscript.

Notes

The authors declare no competing financial interest.

■ ACKNOWLEDGMENTS

P.N.N. thanks Swiss National Science Foundation (SNF) Spark funding (grant number: CRSK-2-190330). S.C. acknowledges support from SNF for Marie Heim-Vogtlin grant (number: PMPDP3_164425). D.T. acknowledges support from Science Foundation Ireland (SFI) under award number 12/RC/2275_P2 and supercomputing resources at the SFI/Higher Education Authority Irish Center for High-End Computing (ICHEC). The authors acknowledge Prof. Roland Riek (ETH Zurich) for the kind permission to access his laboratory and facilities for the production and purification of α-Syn. P.N.N. and O.S. thank Prof. Michel Calame (Empa) for providing access to the Raman spectroscope.

■ REFERENCES

(1) Gibb, W. R.; Lees, A. J. A comparison of clinical and pathological features of young- and old-onset Parkinson's disease. *Neurology* **1988**, *38*, 1402–1406.

(2) Dorsey, E. R.; Elbaz, A.; Nichols, E.; Abd-Allah, F.; Abdelalim, A.; Adsuar, J. C.; Ansha, M. G.; Brayne, C.; Choi, J.-Y. J.; Collado-Mateo, D.; Dahodwala, N.; Do, H. P.; Edessa, D.; Endres, M.; Fereshtehnejad, S.-M.; Foreman, K. J.; Gankpe, F. G.; Gupta, R.; Hankey, G. J.; Hay, S. I.; Hegazy, M. I.; Hibstu, D. T.; Kasaeian, A.; Khader, Y.; Khalil, I.; Khang, Y.-H.; Kim, Y. J.; Kokubo, Y.; Logroscino, G.; Massano, J.; Ibrahim, N. M.; Mohammed, M. A.; Mohammadi, A.; Moradi-Lakeh, M.; Naghavi, M.; Nguyen, B. T.; Nirayo, Y. L.; Ogbo, F. A.; Owolabi, M. O.; Pereira, D. M.; Postma, M. J.; Qorbani, M.; Rahman, M. A.; Roba, K. T.; Safari, H.; Safiri, S.; Satpathy, M.; Sawhney, M.; Shafieesabet, A.; Shiferaw, M. S.; Smith, M.; Szoeke, C. E. I.; Tabarés-Seisdedos, R.; Truong, N. T.; Ukwaja, K. N.; Venketasubramanian, N.; Villafaina, S.; Weldegwergs, K. G.; Westerman, R.; Wijeratne, T.; Winkler, A. S.; Xuan, B. T.; Yonemoto, N.; Feigin, V. L.; Vos, T.; Murray, C. J. L.; et al. Global, regional, and national burden of Parkinson's disease, 1990–2016: a systematic analysis for the Global Burden of Disease Study 2016. *Lancet Neurol.* **2018**, *17*, 939–953.

(3) Warner, T. T.; Schapira, A. H. Genetic and environmental factors in the cause of Parkinson's disease. *Ann. Neurol.* **2003**, *53*, S16–S25.

(4) Bjorklund, G.; Stejskal, V.; Urbina, M. A.; Dadar, M.; Chirumbolo, S.; Mutter, J. Metals and Parkinson's Disease: Mechanisms and Biochemical Processes. *Curr. Med. Chem.* **2018**, *25*, 2198–2214.

(5) Stefanis, L. α-Synuclein in Parkinson's disease. *Cold Spring Harbor Perspect. Med.* **2012**, *2*, No. a009399.

(6) Visanji, N. P.; Lang, A. E.; Kovacs, G. G. Beyond the synucleinopathies: alpha synuclein as a driving force in neurodegenerative comorbidities. *Transl. Neurodegener.* **2019**, *8*, No. 28.

(7) Twohig, D.; Nielsen, H. M. α-synuclein in the pathophysiology of Alzheimer's disease. *Mol. Neurodegener.* **2019**, *14*, No. 23.

(8) Hong, Z.; Shi, M.; Chung, K. A.; Quinn, J. F.; Peskind, E. R.; Galasko, D.; Jankovic, J.; Zabetian, C. P.; Leverenz, J. B.; Baird, G.; Montine, T. J.; Hancock, A. M.; Hwang, H.; Pan, C.; Bradner, J.; Kang, U. J.; Jensen, P. H.; Zhang, J. DJ-1 and α-synuclein in human cerebrospinal fluid as biomarkers of Parkinson's disease. *Brain* **2010**, *133*, 713–726.

(9) Wineman-Fisher, V.; Bloch, D. N.; Miller, Y. Challenges in studying the structures of metal-amyloid oligomers related to type 2 diabetes, Parkinson's disease, and Alzheimer's disease. *Coord. Chem. Rev.* **2016**, *327–328*, 20–26.

(10) Pall, H. S.; Blake, D. R.; Gutteridge, J. M.; Williams, A. C.; Lunec, J.; Hall, M.; Taylor, A. Raised cerebrospinal-fluid copper concentration in Parkinson's disease. *Lancet* **1987**, *330*, 238–241.

(11) Santos, J.; Gracia, P.; Navarro, S.; Peña-Díaz, S.; Pujols, J.; Cremades, N.; Pallarès, I.; Ventura, S. alpha-Helical peptidic scaffolds to target alpha-synuclein toxic species with nanomolar affinity. *Nat. Commun.* **2021**, *12*, No. 3752.

(12) Du, X. Y.; Xie, X. X.; Liu, R. T. The Role of alpha-Synuclein Oligomers in Parkinson's Disease. *Int. J. Mol. Sci.* **2020**, *21*, No. 8645.
(13) Ingelsson, M. Alpha-Synuclein Oligomers-Neurotoxic Molecules in Parkinson's Disease and Other Lewy Body Disorders. *Front. Neurosci.* **2016**, *10*, No. 408.
(14) Ray, S.; Singh, N.; Kumar, R.; Patel, K.; Pandey, S.; Datta, D.; Mahato, J.; Panigrahi, R.; Navalkar, A.; Mehra, S.; Gadhe, L.; Chatterjee, D.; Sawner, A. S.; Maiti, S.; Bhatia, S.; Gerez, J. A.; Chowdhury, A.; Kumar, A.; Padinhateeri, R.; Riek, R.; Krishnamoorthy, G.; Maji, S. K. α-Synuclein aggregation nucleates through liquid−liquid phase separation. *Nat. Chem.* **2020**, *12*, 705−716.
(15) Buell, A. K.; Galvagnion, C.; Gaspar, R.; Sparr, E.; Vendruscolo, M.; Knowles, T. P.; Linse, S.; Dobson, C. M. Solution conditions determine the relative importance of nucleation and growth processes in alpha-synuclein aggregation. *Proc. Natl. Acad. Sci. U.S.A.* **2014**, *111*, 7671−7676.
(16) Boylan, L. S.; Chiò, A. Divining progression in Parkinson disease with a blood test. *Neurology* **2019**, *93*, 471−472.
(17) Lowe, R.; Pountney, D. L.; Jensen, P. H.; Gai, W. P.; Voelcker, N. H. Calcium(II) selectively induces alpha-synuclein annular oligomers via interaction with the C-terminal domain. *Protein Sci.* **2009**, *13*, 3245−3252.
(18) Rasia, R. M.; Bertoncini, C. W.; Marsh, D.; Hoyer, W.; Cherny, D.; Zweckstetter, M.; Griesinger, C.; Jovin, T. M.; Fernández, C. O. Structural characterization of copper(II) binding to α-synuclein: Insights into the bioinorganic chemistry of Parkinson's disease. *Proc. Natl. Acad. Sci. U.S.A.* **2005**, *102*, 4294−4299.
(19) Choi, T. S.; Lee, J.; Han, J. Y.; Jung, B. C.; Wongkongkathep, P.; Loo, J. A.; Lee, M. J.; Kim, H. I. Supramolecular Modulation of Structural Polymorphism in Pathogenic alpha-Synuclein Fibrils Using Copper(II) Coordination. *Angew. Chem., Int. Ed.* **2018**, *57*, 3099−3103.
(20) Binolfi, A.; Rasia, R. M.; Bertoncini, C. W.; Ceolin, M.; Zweckstetter, M.; Griesinger, C.; Jovin, T. M.; Fernandez, C. O. Interaction of alpha-synuclein with divalent metal ions reveals key differences: a link between structure, binding specificity and fibrillation enhancement. *J. Am. Chem. Soc.* **2006**, *128*, 9893−9901.
(21) Wright, J. A.; Wang, X.; Brown, D. R. Unique copper-induced oligomers mediate alpha-synuclein toxicity. *FASEB J.* **2009**, *23*, 2384−2393.
(22) Wang, X.; Moualla, D.; Wright, J. A.; Brown, D. R. Copper binding regulates intracellular alpha-synuclein localisation, aggregation and toxicity. *J. Neurochem.* **2010**, *113*, 704−714.
(23) Ruggeri, F. S.; Benedetti, F.; Knowles, T. P. J.; Lashuel, H. A.; Sekatskii, S.; Dietler, G. Identification and nanomechanical characterization of the fundamental single-strand protofilaments of amyloid α-synuclein fibrils. *Proc. Natl. Acad. Sci. U.S.A.* **2018**, *115*, 7230−7235.
(24) Sweers, K. K. M.; Segers-Nolten, I. M. J.; Bennink, M. L.; Subramaniam, V. Structural model for α-synuclein fibrils derived from high resolution imaging and nanomechanical studies using atomic force microscopy. *Soft Matter* **2012**, *8*, 7215−7222.
(25) Fink, A. L. The aggregation and fibrillation of alpha-synuclein. *Acc. Chem. Res.* **2006**, *39*, 628−634.
(26) Erickson, H. P. Size and Shape of Protein Molecules at the Nanometer Level Determined by Sedimentation, Gel Filtration, and Electron Microscopy. *Biol. Proced. Online* **2009**, *11*, No. 32.
(27) Zhang, Y.; Hashemi, M.; Lv, Z.; Williams, B.; Popov, K. I.; Dokholyan, N. V.; Lyubchenko, Y. L. High-speed atomic force microscopy reveals structural dynamics of α-synuclein monomers and dimers. *J. Chem. Phys.* **2018**, *148*, No. 123322.
(28) Nirmalraj, P. N.; List, J.; Battacharya, S.; Howe, G.; Xu, L.; Thompson, D.; Mayer, M. Complete aggregation pathway of amyloid β (1-40) and (1-42) resolved on an atomically clean interface. *Sci. Adv.* **2020**, *6*, No. eaaz6014.
(29) Flynn, J. D.; McGlinchey, R. P.; Walker, R. L., 3rd; Lee, J. C. Structural features of α-synuclein amyloid fibrils revealed by Raman spectroscopy. *J. Biol. Chem.* **2018**, *293*, 767−776.
(30) Apetri, M. M.; Maiti, N. C.; Zagorski, M. G.; Carey, P. R.; Anderson, V. E. Secondary structure of alpha-synuclein oligomers: characterization by raman and atomic force microscopy. *J. Mol. Biol.* **2006**, *355*, 63−71.
(31) Makky, A.; Bousset, L.; Polesel-Maris, J.; Melki, R. Nanomechanical properties of distinct fibrillar polymorphs of the protein α-synuclein. *Sci. Rep.* **2016**, *6*, No. 37970.
(32) Shin, E. J.; Park, J. W. Nanoaggregates Derived from Amyloid-beta and Alpha-synuclein Characterized by Sequential Quadruple Force Mapping. *Nano Lett.* **2021**, *21*, 3789−3797.
(33) Ruggeri, F. S.; Flagmeier, P.; Kumita, J. R.; Meisl, G.; Chirgadze, D. Y.; Bongiovanni, M. N.; Knowles, T. P. J.; Dobson, C. M. The Influence of Pathogenic Mutations in α-Synuclein on Biophysical and Structural Characteristics of Amyloid Fibrils. *ACS Nano* **2020**, *14*, 5213−5222.
(34) Devitt, G.; Howard, K.; Mudher, A.; Mahajan, S. Raman Spectroscopy: An Emerging Tool in Neurodegenerative Disease Research and Diagnosis. *ACS Chem. Neurosci.* **2018**, *9*, 404−420.
(35) Signorelli, S.; Cannistraro, S.; Bizzarri, A. R. Raman Evidence of p53-DBD Disorder Decrease upon Interaction with the Anticancer Protein Azurin. *Int. J. Mol. Sci.* **2019**, *20*, No. 3078.
(36) Tian, Y.; Stanyon, H. F.; Barritt, J. D.; Mayet, U.; Patel, P.; Karamani, E.; Fusco, G.; Viles, J. H. Copper(2+) Binding to alpha-Synuclein. Histidine50 Can Form a Ternary Complex with Cu(2+) at the N-Terminus but Not a Macrochelate. *Inorg. Chem.* **2019**, *58*, 15580−15589.
(37) Lorentzon, E.; Kumar, R.; Horvath, I.; Wittung-Stafshede, P. Differential effects of Cu(2+) and Fe(3+) ions on in vitro amyloid formation of biologically-relevant α-synuclein variants. *BioMetals* **2020**, *33*, 97−106.
(38) Tuttle, M. D.; Comellas, G.; Nieuwkoop, A. J.; Covell, D. J.; Berthold, D. A.; Kloepper, K. D.; Courtney, J. M.; Kim, J. K.; Barclay, A. M.; Kendall, A.; Wan, W.; Stubbs, G.; Schwieters, C. D.; Lee, V. M. Y.; George, J. M.; Rienstra, C. M. Solid-state NMR structure of a pathogenic fibril of full-length human alpha-synuclein. *Nat. Struct. Mol. Biol.* **2016**, *23*, 409−415.
(39) Nguyen, P. H.; Ramamoorthy, A.; Sahoo, B. R.; Zheng, J.; Faller, P.; Straub, J. E.; Dominguez, L.; Shea, J. E.; Dokholyan, N. V.; De Simone, A.; Ma, B.; Nussinov, R.; Najafi, S.; Ngo, S. T.; Loquet, A.; Chiricotto, M.; Ganguly, P.; McCarty, J.; Li, M. S.; Hall, C.; Wang, Y.; Miller, Y.; Melchionna, S.; Habenstein, B.; Timr, S.; Chen, J.; Hnath, B.; Strodel, B.; Kayed, R.; Lesné, S.; Wei, G.; Sterpone, F.; Doig, A. J.; Derreumaux, P. Amyloid Oligomers: A Joint Experimental/Computational Perspective on Alzheimer's Disease, Parkinson's Disease, Type II Diabetes, and Amyotrophic Lateral Sclerosis. *Chem. Rev.* **2021**, *121*, 2545−2647.
(40) Nguyen, P. H.; Derreumaux, P. Structures of the intrinsically disordered Abeta, tau and alpha-synuclein proteins in aqueous solution from computer simulations. *Biophys. Chem.* **2020**, *264*, No. 106421.
(41) Lan-Mark, S.; Miller, Y. Insights into the Interactions that Trigger the Primary Nucleation of Polymorphic alpha-Synuclein Dimers. *ACS Chem. Neurosci.* **2022**, *13*, 370−378.
(42) Bhattacharya, S.; Xu, L.; Thompson, D. Revisiting the earliest signatures of amyloidogenesis: Roadmaps emerging from computational modeling and experiment. *WIREs Comput. Mol. Sci.* **2018**, *8*, No. e1359.
(43) Xu, L.; Bhattacharya, S.; Thompson, D. Re-designing the alpha-synuclein tetramer. *Chem. Commun.* **2018**, *54*, 8080−8083.
(44) Bhattacharya, S.; Xu, L.; Thompson, D. Molecular Simulations Reveal Terminal Group Mediated Stabilization of Helical Conformers in Both Amyloid-beta42 and alpha-Synuclein. *ACS Chem. Neurosci.* **2019**, *10*, 2830−2842.
(45) Bhattacharya, S.; Xu, L.; Thompson, D. Long-range Regulation of Partially Folded Amyloidogenic Peptides. *Sci. Rep.* **2020**, *10*, No. 7597.
(46) Bellucci, L.; Bussi, G.; Di Felice, R.; Corni, S. , Fibrillation-prone conformations of the amyloid-beta-42 peptide at the gold/water interface. *Nanoscale* **2017**, *9*, 2279−2290.

https://doi.org/10.1021/acschemneuro.2c00021
ACS Chem. Neurosci. 2022, 13, 1410−1421

(47) Bloch, D. N.; Kolkowska, P.; Tessari, I.; Baratto, M. C.; Sinicropi, A.; Bubacco, L.; Mangani, S.; Pozzi, C.; Valensin, D.; Miller, Y. Fibrils of alpha-Synuclein Abolish the Affinity of Cu(2+)-Binding Site to His50 and Induce Hopping of Cu(2+) Ions in the Termini. *Inorg. Chem.* **2019**, *58*, 10920−10927.
(48) Chen, S. W.; Drakulic, S.; Deas, E.; Ouberai, M.; Aprile, F. A.; Arranz, R.; Ness, S.; Roodveldt, C.; Guilliams, T.; De-Genst, E. J.; Klenerman, D.; Wood, N. W.; Knowles, T. P.; Alfonso, C.; Rivas, G.; Abramov, A. Y.; Valpuesta, J. M.; Dobson, C. M.; Cremades, N. Structural characterization of toxic oligomers that are kinetically trapped during alpha-synuclein fibril formation. *Proc. Natl. Acad. Sci. U.S.A.* **2015**, *112*, E1994−E2003.
(49) Lashuel, H. A.; Hartley, D.; Petre, B. M.; Walz, T.; Lansbury, P. T., Jr. Neurodegenerative disease: amyloid pores from pathogenic mutations. *Nature* **2002**, *418*, No. 291.
(50) Lashuel, H. A.; Petre, B. M.; Wall, J.; Simon, M.; Nowak, R. J.; Walz, T.; Lansbury, P. T., Jr. α-Synuclein, especially the Parkinson's disease-associated mutants, forms pore-like annular and tubular protofibrils. *J. Mol. Biol.* **2002**, *322*, 1089−1102.
(51) Paslawski, W.; Mysling, S.; Thomsen, K.; Jørgensen, T. J.; Otzen, D. E. Co-existence of two different alpha-synuclein oligomers with different core structures determined by hydrogen/deuterium exchange mass spectrometry. *Angew. Chem., Int. Ed.* **2014**, *53*, 7560−7563.
(52) Salveson, P. J.; Spencer, R. K.; Nowick, J. S. X-ray Crystallographic Structure of Oligomers Formed by a Toxic beta-Hairpin Derived from alpha-Synuclein: Trimers and Higher-Order Oligomers. *J. Am. Chem. Soc.* **2016**, *138*, 4458−4467.
(53) Zou, Y.; Qian, Z.; Gong, Y.; Tang, Y.; Wei, G.; Zhang, Q. Critical nucleus of Greek-key-like core of alpha-synuclein protofibril and its disruption by dopamine and norepinephrine. *Phys. Chem. Chem. Phys.* **2020**, *22*, 203−211.
(54) Alam, P.; Bousset, L.; Melki, R.; Otzen, D. E. alpha-synuclein oligomers and fibrils: a spectrum of species, a spectrum of toxicities. *J. Neurochem.* **2019**, *150*, 522−534.
(55) Cremades, N.; Chen, S. W.; Dobson, C. M. Structural Characteristics of alpha-Synuclein Oligomers. *Int. Rev. Cell Mol. Biol.* **2017**, *329*, 79−143.
(56) Nirmalraj, P. N.; Schneider, T.; Felbecker, A. Spatial organization of protein aggregates on red blood cells as physical biomarkers of Alzheimer's disease pathology. *Sci. Adv.* **2021**, *7*, No. eabj2137.
(57) Campioni, S.; Carret, G.; Jordens, S.; Nicoud, L.; Mezzenga, R.; Riek, R. The Presence of an Air−Water Interface Affects Formation and Elongation of α-Synuclein Fibrils. *J. Am. Chem. Soc.* **2014**, *136*, 2866−2875.
(58) Binolfi, A.; Rodriguez, E. E.; Valensin, D.; D'Amelio, N.; Ippoliti, E.; Obal, G.; Duran, R.; Magistrato, A.; Pritsch, O.; Zweckstetter, M.; Valensin, G.; Carloni, P.; Quintanar, L.; Griesinger, C.; Fernández, C. O. Bioinorganic chemistry of Parkinson's disease: structural determinants for the copper-mediated amyloid formation of alpha-synuclein. *Inorg. Chem.* **2010**, *49*, 10668−10679.

https://doi.org/10.1021/acschemneuro.2c00021
ACS Chem. Neurosci. 2022, 13, 1410−1421